

Superfluid transitions and capillary condensation in porous media

R. J. Lazarowich and P. Taborek

Department of Physics and Astronomy, University of California, Irvine, California 92697, USA

(Received 1 May 2006; published 17 July 2006)

We report experimental results on the superfluid onset of ^4He adsorbed onto two types of porous material: porous gold and evaporated CaF_2 . Films of these materials in a range from 0.008 to 4 microns thick were deposited onto the surfaces of quartz microbalances. The microbalances were used to measure helium adsorption and desorption isotherms on the porous substrates in the range of 1 to 3 K. Isotherms on a nominally flat Au substrate are included for comparison. The isotherms were used to construct phase diagrams in the μ - T plane showing hysteresis closure points and superfluid onsets. Hysteresis loops were observed in all of the porous gold samples. Thin CaF_2 films behaved like rough surfaces with an enhanced adsorption area but no hysteresis, while CaF_2 films thicker than approximately 0.04 microns behaved like porous materials and exhibited hysteresis. The characteristics of superfluid onset in the porous samples depended crucially on whether the transition occurred at low coverage and low temperature in the single phase regime, or at higher temperatures and coverage in the hysteretic two phase regime. In the single phase regime, superfluid onset showed both the abrupt frequency shift and dissipation peak characteristic of a conventional Kosterlitz-Thouless transition, corrected for the increased area and tortuosity of the substrate. At higher temperatures and coverages, a dissipation peak is observed, but the nearly discontinuous frequency shift is replaced by a smooth and gradual decoupling of the superfluid component as the coverage is increased. The gradual onset of superflow can be approximately described by a power law with an exponent near 1.5.

DOI: [10.1103/PhysRevB.74.024512](https://doi.org/10.1103/PhysRevB.74.024512)

PACS number(s): 67.70.+n, 64.70.Ja, 67.40.Hf, 67.40.Pm

I. INTRODUCTION

The phase behavior of helium in porous materials has been of considerable interest because it provides a means of changing the effective density, altering the interactions and introducing disorder into liquid helium, and observing the effects of these changes on the superfluid transition. The most extensive studies have utilized either Vycor glass, aerogel, nuclepore or alumina powder as the porous substrate. Experimental probes have included conventional ultrasound,¹ third sound,² fourth sound,^{3,4} fifth sound,⁵ capacitance^{6,7} and torsional oscillators.^{8,9} The focus of most^{10,11} of this work has been either the low coverage, low temperature regime where the pores do not contain bulk fluid, or the regime near T_λ with full pores.

Adsorption on the surfaces of a rough or porous substrate often involves capillary condensation, in which the dense liquid phase is stabilized in cracks and pores under thermodynamic conditions for which the bulk liquid phase would be unstable. For example, a cylindrical mesopore of radius r with a thin adsorbed film will completely fill with liquid at a chemical potential lower than the bulk coexistence value by an amount $\Delta\mu = -v_l\sigma_{lg}/r$, where v_l is the molar volume of the liquid and σ_{lg} is the liquid-vapor surface tension. The thermodynamic cost of stabilizing liquid below the saturated vapor pressure is compensated by the elimination of the internal liquid-vapor interface in the filled pore, which lowers the surface energy. Capillary condensation has many features of a first order phase transition. There is a nearly discontinuous jump in the order parameter at the transition, and the transition is typically hysteretic. The fluid in a filled cylindrical capillary will not drain until the chemical potential offset reaches $\Delta\mu = -2v_l\sigma_{lg}/r$, which is twice the value required to fill it. In real materials, both the inevitable distri-

bution of pore sizes and the interconnectivity of the pores complicates the analysis of the hysteresis. This hysteresis is clearly visible in the difference between adsorption isotherms obtained by adding vapor and increasing the pressure, and those obtained by removing vapor and decreasing the pressure, as shown in Figs. 8 and 10(b). The hysteresis loop defines a regime in which the total adsorbed mass is not a single valued function of the pressure or chemical potential, but rather is history dependent.

The endpoints of the hysteresis loops define two curves in the $\Delta\mu$ - T plane, as shown in the generic phase diagram of Fig. 1. Superfluid onset at coexistence ($\Delta\mu=0$) and at low coverage ($\Delta\mu\ll 0$) have been extensively studied, and the transition can be described in terms of either finite size effects or the conventional two-dimensional (2D) Kosterlitz-Thouless (KT) transition. The purpose of this work is to explore superfluid onset in the intermediate region in which full and empty pores coexist.

Much of the previous work on helium in porous media has employed torsional oscillators with closed cells which are filled with porous substrate and have essentially no dead volume. This type of oscillator can detect superfluid onset, but cannot distinguish between liquid and vapor since all nonsuperfluid contributes to the inertia. This type of detector is typically operated at fixed total number of atoms, N , and the superfluid transition is crossed by varying T . The interpretation of the oscillator data is particularly straightforward at low temperatures where the number of atoms in the gas phase is negligible, or when the cell is entirely full of liquid. Recently, several groups have pioneered techniques to fabricate porous substrates on quartz crystal microbalances (QCMs).^{2,12} We have used these techniques to cover the QCM electrodes with porous gold and with rough or porous films of CaF_2 . The QCMs are operated in diffusive contact

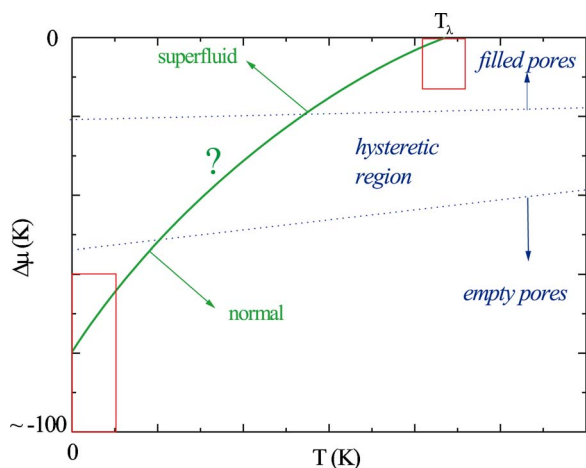


FIG. 1. (Color online) Schematic phase diagram in the $\Delta\mu$ - T plane for helium adsorbed on a porous medium, where $\Delta\mu$ is the chemical potential offset from bulk coexistence. The solid curve separates regions of vanishing and nonvanishing superfluid density. This curve intersects the $\Delta\mu=0$ axis at T_λ . The nearly parallel dotted lines are the boundaries of the region of hysteretic adsorption and desorption where the pores are partially filled with liquid. The exact size and shape of this capillary condensation region depends on the pore structure of the medium, but the dotted lines generally intersect near the bulk critical point. The boxes highlight the region of the phase diagram where most previous work has been carried out.

with a large reservoir of vapor at a fixed temperature, T , so the natural control parameters are the reservoir pressure, P , or equivalently, the chemical potential offset from coexistence $\Delta\mu$. Like conventional torsional oscillators, QCMs also detect all nonsuperfluid in the pores, but capillary condensation can be inferred by comparing forward and reverse adsorption isotherms. These can be conveniently measured at temperatures above 1 K where the vapor pressure is sufficiently high. The measurements reported here complement previous low temperature, low coverage torsional oscillator work.

The paper is organized as follows: Section II describes the QCM setup and documents the ability to reproduce well-known features of the KT transition on a nominally flat nonporous gold substrate. The techniques for fabricating the porous substrates and measuring properties such as porosity, surface area and the superfluid drag coefficient χ are also described. Section III describes the unusual signatures of superfluid onset we observe in both porous Au and CaF_2 when the transition occurs within the hysteretic regime. Section IV presents a summary and discussion of the observations.

II. EXPERIMENT

A. QCM measurements

The QCMs employed in this experiment were made from SC-cut quartz with nominally flat Au electrodes. They oscillate in vacuum at 5.5 MHz in the fundamental shear mode with a quality factor (Q) of 6×10^4 . The resonance frequency of a QCM changes due to the adsorption of a film of areal mass density, σ , given by

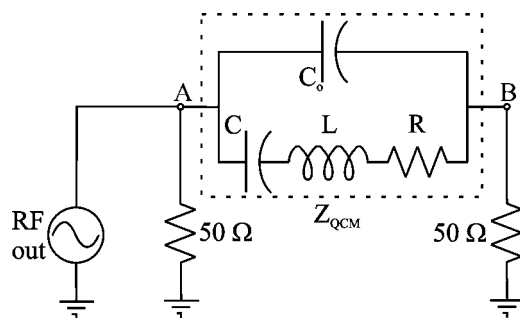


FIG. 2. Circuit diagram of a QCM in resonance connected to a network analyzer. Typical values for the circuit parameters are $C_0 = 7.1$ pF, $L = 83.8$ mH, $R = 60 \Omega$, $C = 0.01$ pF.

$$\Delta\nu = -2 \left(\frac{2\nu_o^2}{nZ} \right) \sigma, \quad (1)$$

where $\Delta\nu$ is the total frequency shift, n is the mode of vibration ($n=1$ for our QCM), ν_o is the vacuum resonance frequency, and Z is the acoustic impedance of the crystal ($Z = 9.51 \times 10^6$ kg/m² s).¹³ The extra factor of 2 compensates for liquid loading on both electrodes. The resonance frequency also changes due to viscous coupling to the vapor¹⁴ and hydrostatic compression;¹⁵ all the data presented here have been corrected for these effects. No additional corrections were made for the gas trapped inside the porous structure because the vapor density was always less than 1% of the liquid value, which rendered the effect negligible.

Figure 2 shows the electrical equivalent circuit of the QCM as well as the components of the network analyzer that is used to measure the crystal properties. The HP 4197A network analyzer that we use applies a radio frequency signal of amplitude 2.2 mV across the QCM which is also connected to two voltage sampling ports at A and B with 50 Ω input impedance. The ratio of the voltages at A and B is simply determined by the impedance Z_{QCM} of the QCM:

$$\frac{V_B}{V_A} = \frac{50}{Z_{\text{QCM}} + 50}. \quad (2)$$

Near resonance, Z_{QCM} is approximately 50 Ω , but it increases rapidly on either side of the resonance. Plots of the voltage amplitude ratio given in Eq. (2) as a function of frequency are approximately Lorentzian curves, as shown, for example, in Fig. 7. Construction of an isotherm involved measuring a resonance curve for each value of the helium vapor pressure in the cell. The curves were fit to the equivalent circuit model with L , C , and R , as free parameters. The frequency corresponding to the maximum in the resonance curves is given to a very good approximation by $\nu_{\text{max}} = 1/(2\pi\sqrt{LC})$. For each temperature, ν_{max} was determined at $P=0$. The primary data we report are the values of $\Delta\nu$, the variation of the resonance frequency from its vacuum value, and R , which describes the height and width of the resonance. The typical precision of these quantities is 0.05 Hz and 0.005 Ω . The measured response values also depend on the length of coaxial cables used to connect the network

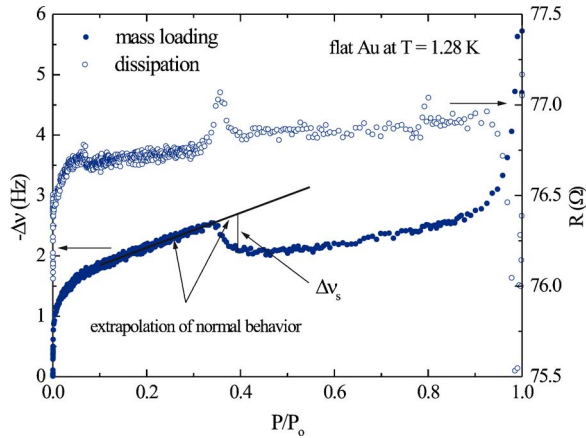


FIG. 3. (Color online) Helium isotherm on nominally flat gold at $T=1.28$ K, showing the frequency shift $-\Delta\nu$ (filled circles, left-hand axis) and the effective resistance R which measures the dissipation (open circles, right-hand axis). The 1.2 Hz increase in $-\Delta\nu$ near $P/P_0=0$ is associated with the solid-like layers of helium that bind strongly to the gold surface. The subsequent approximately linear increase in mass is due to adsorbed liquid helium. The features near $P/P_0=0.34$, which show decoupling of the superfluid fraction and a peak in the dissipation, are the conventional signatures of a KT transition.

analyzer to the QCM, and therefore care was taken to minimize their length.

B. Flat gold

Superfluid transitions in thin films on strong binding substrates have been shown to be of Kosterlitz-Thouless type,¹⁶ which are experimentally characterized on shear-mode QCMs by a nearly discontinuous unloading of superfluid mass at the transition point.^{17,18} A sharp peak in dissipation due to diffusion of vortex cores is also a characteristic feature of the transition.¹⁹ The KT theory predicts that the jump in the superfluid mass density at the transition depends only on the temperature and is given universally by

$$\sigma_s = \frac{8\pi m^2 k_B}{h^2} T_c = \beta T_c, \quad (3)$$

where k_B is Boltzmann's constant, m is the mass of a helium atom, h is Planck's constant, and σ_s is the areal superfluid density at the transition point at the critical temperature, T_c .

Figure 3 shows an isotherm on flat Au at 1.28 K which shows the typical features of superfluid onset. Since the QCM oscillates in the shear mode, it is only sensitive to the viscously coupled normal fraction of helium. At the transition, the superfluid fraction abruptly decouples from the oscillator and causes a shift in the frequency. The superfluid fraction can be determined by measuring the difference between the actual frequency in the superfluid state and the extrapolated frequency in the normal state. The shift due to the transition is given by

$$\Delta\nu_s = \Delta\nu_a - \Delta\nu_e, \quad (4)$$

where $\Delta\nu_a$ is the actual measured change in frequency due to an adsorbed film and $\Delta\nu_e$ is the extrapolated frequency as

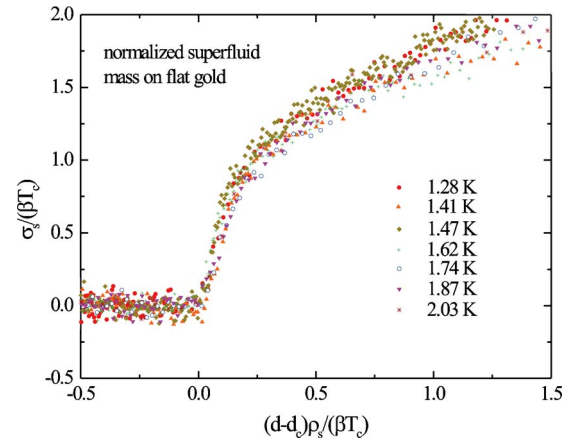


FIG. 4. (Color online) The normalized superfluid density σ_s as a function of the normalized bulk superfluid density $(d-d_c)\rho_s$ for a range of temperatures from 1.28 K to 2.03 K. There is an abrupt jump in the superfluid density at $d=d_c$, followed by an increase linear in d . A conversion of 0.66 Hz = 3.57 Å is used per layer.

indicated by the straight line in Fig. 3. Applying Eqs. (1) and (4) yields the superfluid areal mass density

$$\sigma_s = \frac{nZ}{4\nu_0^2} (\Delta\nu_s). \quad (5)$$

We have measured several isotherms like that shown in Fig. 3 for $1.3 < T < T_\lambda$. As the temperature increases, the superfluid transition occurs for larger values of P/P_0 and film thickness, and the size of the jump in apparent mass also increases. The superfluid fraction for film thickness d greater than the critical film thickness d_c also depends on temperature. The temperature dependence can be simply expressed using dimensionless variables defined by the ratio of the observed superfluid density σ_s to the superfluid density at onset obtained from Eq. (3), βT_c , and the ratio of the superfluid density assuming bulk behavior, $(d-d_c)\rho_s$, to βT_c , where d is the film thickness, d_c is the critical thickness at onset, and ρ_s is the bulk superfluid fraction at T_c . Using these variables, the data for a range of temperatures can be approximately collapsed onto a common curve, as shown in Ref. 20. Our data plotted in this way are shown in Fig. 4. If the scaling was exact, the data would have a discontinuity of unit magnitude at $d=d_c$, with a linear increase with slope = 1 for $d > d_c$. The figure shows that the data closely approximates this behavior, and confirms that our experimental technique and methods of data analysis quantitatively reproduces the expected results for the superfluid transition on a nominally flat surface.

The only parameter involved in this analysis which is not determined by fundamental constants or bulk properties is the film thickness at onset, d_c . There are two other important lengths in the problem which help to determine d_c . One is d_0 , the thickness of the solidlike “dead” layer which is formed on typical strong substrates and does not participate in superfluidity. The other is the bulk transverse correlation length, $\xi(T)$, given by the Josephson expression²¹

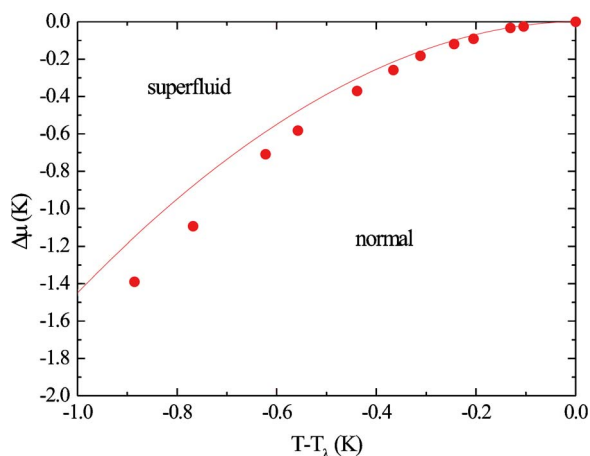


FIG. 5. (Color online) Location of superfluid onsets in the $\Delta\mu$ - T plane for helium on flat Au. Dots are from data such as Fig. 3. Dashed curve is from Eqs. (12) and (10).

$$\xi(T) = \frac{4\pi^2 m^2 k_B T}{h^2 \rho_s(T)}. \quad (6)$$

d_c must be larger than either of these lengths, and a plausible estimate is that $d_c \sim d_0 + \xi(T)$. At high temperatures near T_λ , $\xi(T) \gg d_0$, so the approximation $d_c \sim \xi(T)$ is valid. Near T_λ , $\rho_s(T)$ depends on temperature as

$$\rho_s(t) = \rho_0 t^{2/3}, \quad (7)$$

where the reduced temperature, t , is defined as

$$t = \frac{T_\lambda - T}{T_\lambda}. \quad (8)$$

These relations imply that near T_λ , the correlation length can be approximated by

$$\xi(t) = \xi_0 t^{-2/3}. \quad (9)$$

For most of our work, the chemical potential at superfluid onset $\Delta\mu_c$ is a more convenient variable than d_c . The relationship between them can be approximated by

$$\Delta\mu_c = -\frac{\alpha}{d_c^3}, \quad (10)$$

where α is the van der Waals constant, with $\alpha = 3100 \text{ K \AA}^3$ for helium on gold.²² Combining the relation $d_c \sim \xi(T)$ with Eqs. (9) and (10) yields

$$\Delta\mu_c \propto -\frac{\alpha}{\xi_0^3 t^2} \quad (11)$$

so $\Delta\mu_c$ should be a quadratic function of t near T_λ . The data points in Fig. 5 show that this is qualitatively correct even for $t \approx 0.5$.

At low temperatures $T \approx 0$, $t \approx 1$, the approximations of Eqs. (7) and (9) are no longer valid. In this regime, ρ_s is independent of temperature, and $\xi(T)$ is proportional to T and vanishes as $T \rightarrow 0$, so $d_c \approx d_0$. A useful interpolation formula that connects the low and high temperature regimes can be constructed using the parametrization

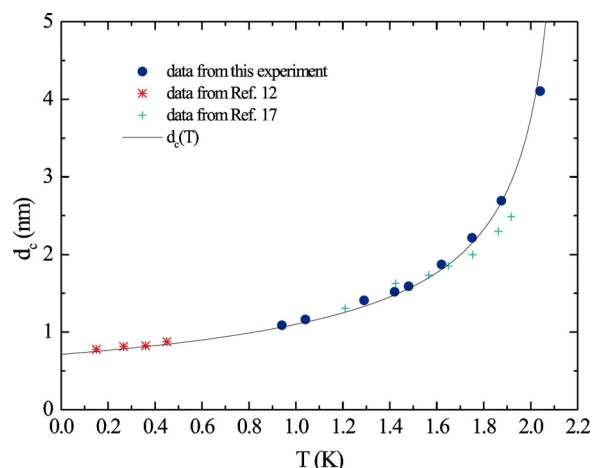


FIG. 6. (Color online) Values of d_c in nm from our data, Ref. 12, and Ref. 17. The curve is $d_c(T) = (0.76 + 0.46 T)\xi(T) + 0.71$. The fit is constructed using data from this work and Ref. 12.

$$d_c(T) = (a + bT)\xi(T) + d_0. \quad (12)$$

Values of $d_0 = 0.71 \text{ nm}$, $a = 0.76$, and $b = 0.46 \text{ K}^{-1}$ reproduce both our high temperature results and the low temperature results of Ref. 12, as shown in Fig. 6. Similar analyses covering various temperature regimes have been presented previously.^{23–26}

Equation (12) together with the analysis underlying Fig. 4 constitute a good approximate description of the position and shape of the oscillator response on a flat gold substrate near the superfluid transition throughout the temperature range $0 < T < T_\lambda$.

C. Preparation and properties of porous substrates

1. Porous gold

Porous gold substrates were prepared as described in Ref. 12 by sputtering an alloy of silver and gold onto both sides of the flat Au electrodes of the QCMs. The sputtering target was a conventional 2 inch Ag target with millimeter sized pieces of pure Au spread out randomly on the Ag surface. The number of Au pieces was adjusted so that the sputtered alloy film was approximately 30% Au. The Au/Ag ratio in the deposited film was verified using EDS on a sacrificial sample placed next to the QCM. To finalize the process, the QCM was dipped into 70% nitric acid for approximately 1 minute to selectively etch out the silver. After etching, the surface of the film was black and dull. Figure 7 shows an example of the QCM resonance curve before and after the application of a porous gold film. Although there is a large shift in resonant frequency due to the increased mass, the Q is not significantly degraded.

Several methods are used to determine the physical properties of the porous Au films, all of which are linked to the changes in resonance of the QCMs. The total thickness of the sputtered alloy film is determined using Eq. (1) from the difference in frequency after the sputtering process. Assuming the thickness of the film does not change during etching, the subsequent frequency shift due to the removal of silver

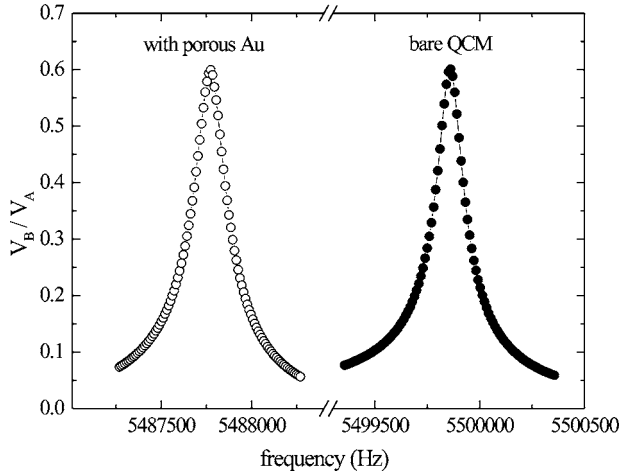


FIG. 7. Comparison of the resonance curves before and after the deposition and etching of porous gold resulting in a frequency difference of 12 060 Hz. Although there is a large frequency shift, the width of the resonance, which measures the Q of the oscillator, is not strongly affected.

yields the total pore volume, V_p , and the porosity, ε , which is the volume fraction of holes. As shown in Table I, typical values of ε are approximately 0.6, which is consistent with the silver concentration of the alloy.

Another measure of the total pore volume comes from the frequency shift corresponding to full pores which occurs at the high pressure closure point of the hysteresis loop, as shown in Fig. 8, which shows a typical experimental isotherm above the bulk lambda point where complications due to superfluidity do not occur. The frequency shift $\Delta\nu_V$ at the closure point is converted into a mass using Eq. (1), and the pore volume is determined assuming the mass is due to liquid at the bulk density. The total pore volume determined in this way is within 10% of the value obtained from the frequency shift due to etching.

The area of the pores was determined by analyzing the nearly vertical initial rise at the low coverage, low pressure end of an isotherm, which is due to approximately two layers of strongly bound, immobile helium. Since the pressures are immeasurably low, the features of this initial step are shown in Fig. 9 for several porous gold samples and a nominally flat gold film as a function of the total helium gas added to the cell in micromoles. The frequency shift at a gas dose of 100 micromoles, $\Delta\nu_A$, provides a measure of the effective surface area of the substrate. The area of the nominally flat electrode was measured using a nitrogen BET isotherm and found to be 1.15 times the geometrical area. Hysteresis loops in po-

TABLE I. Average values for surface area, porosity ε , pore diameter ζ , and superfluid drag coefficient χ of the three porous gold films.

Thickness (nm)	ε	Surface area (cm ²)	ζ (nm)	χ
220	0.56	6.16	22	0.75
1250	0.68	35.42	33	0.67
3310	0.75	51.59	40	0.52

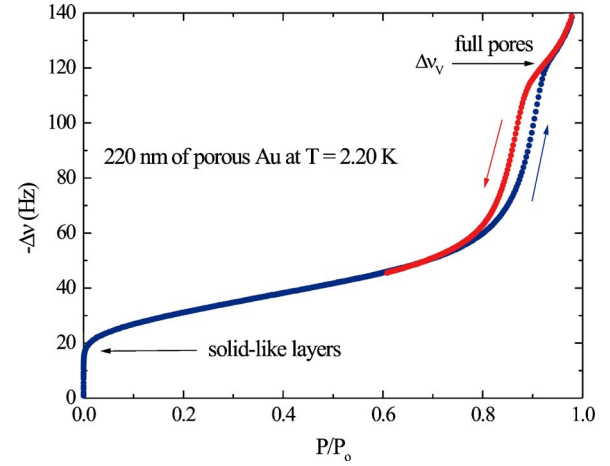


FIG. 8. (Color online) Forward and reverse adsorption of normal helium on porous gold of nominal thickness 220 nm at $T = 2.20$ K, showing $\Delta\nu$ as a function of reduced pressure. The nearly vertical feature at $P=0$ is due to the formation of strongly bound solidlike layers, and can be used to estimate the area of the pores. The closure point of the hysteresis loop corresponds to pore filling, and can be used to estimate the pore volume.

rous gold occur over a relatively narrow range of P/P_0 and have a shape corresponding to a type H1 isotherm,²⁷ which is typical of materials with cylindrical pores. The assumption of cylindrical pores is also consistent with previous work on these porous gold films.¹² If the total length of all the pore channels is L , and the average pore diameter is ζ , the total pore volume V_p is $L\pi\zeta^2/4$ and the total area A_{tot} is $\pi\zeta L$, so the average pore diameter is

$$\zeta = \frac{4V_p}{A_{\text{tot}}}. \quad (13)$$

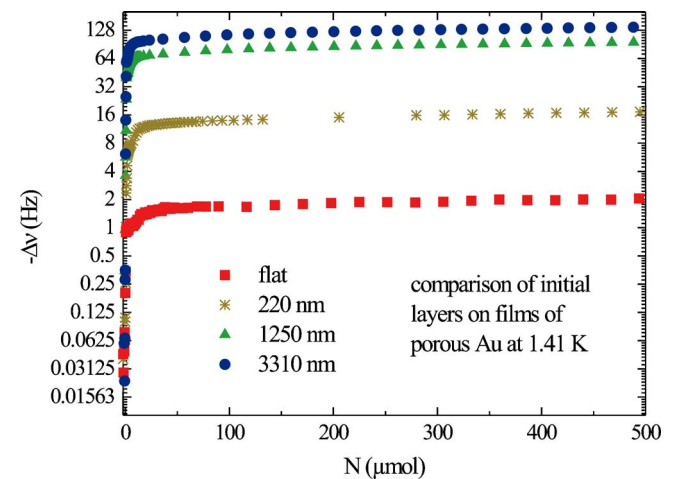


FIG. 9. (Color online) $\Delta\nu$ as a function of the helium dosage N for samples of porous Au of various thicknesses at $T = 1.41$ K. The rapid rise near $N=0$ is due to the formation of approximately two strongly bound layers of solidlike helium. The size of this rise, $\Delta\nu_A$, is a measure of the area of the porous sample. Results for a nominally flat Au substrate are included for comparison.

The quantities in Eq. (13) can be related to measurable features of the isotherms. Using $\Delta\nu_V \propto V_p$ and $\Delta\nu_A \propto A_{\text{tot}}(0.7 \text{ nm})$ where the plateau regions of Fig. 9 are assumed to correspond to a coverage of two layers with a thickness of 0.7 nm, ζ can be expressed as

$$\zeta = \frac{(4)(0.7)\Delta\nu_V}{\Delta\nu_A}. \quad (14)$$

in units of nanometers. Table I summarizes the properties of the porous Au samples.

2. CaF₂

CaF₂ substrates were prepared by thermally evaporating equal amounts of CaF₂ onto both electrodes of a QCM with disposition rates in the range of 6–10 Å/s. The total mass of the CaF₂ films was determined by the frequency shift after evaporation. The various samples are identified by an effective thickness d_{CaF_2} which was computed from the total mass of CaF₂ and the bulk density of CaF₂, which is 3.19 g/cm³. As in the case of porous gold, helium isotherms above the lambda point were used to deduce the geometrical properties of the substrate. For CaF₂, however, isotherms had qualitatively different features for low and high CaF₂ coverage, with a crossover between the two regimes at a nominal thickness of approximately 43 nm. A typical example of an isotherm on a thick CaF₂ substrate is shown in Fig. 10(b), which shows a distinct hysteresis loop which extends over a large range of P/P_0 . The endpoint of the hysteresis loop at high pressures and coverage defines the condition of full pores. The frequency shift at the full pore condition is simply related to the total adsorbed helium mass. The total pore volume V_p and the effective thickness of helium d_{He} can be calculated from the measured mass by assuming that the pores are full of liquid at the bulk density of 0.145 g/cm³. The porosity, ϵ , is defined as $d_{\text{He}}/(d_{\text{He}} + d_{\text{CaF}_2})$.

The surface area of the CaF₂ substrates was determined in a similar manner as the porous gold substrates using the size of the initial step in the isotherm at low coverage, which is shown in Fig. 11. The surface area is a monotonically increasing function of the CaF₂ thickness, even in the range below 43 nm where no hysteresis is observed. For our thickest CaF₂ substrates, the effective surface area determined in this way was over 40 times larger than on a flat gold electrode. Another possible method of determining the surface area of these substrates is to use AFM to map out the topography. The AFM technique was used in several recent studies^{2,28} which concluded that the surface area of a 300 nm thick CaF₂ substrate was approximately 1.2 times larger than a nominally flat surface. We repeated these AFM measurements using our samples and obtained similar results. Use of topographical measurements to estimate the area relies on the assumption that the surface is rough like a mountain landscape rather than porous like a sponge. Our adsorption measurements show that for CaF₂ substrates thicker than 40 nm the spongelike picture is more accurate and that AFM topographical measurements can underestimate the real adsorption area by orders of magnitude.

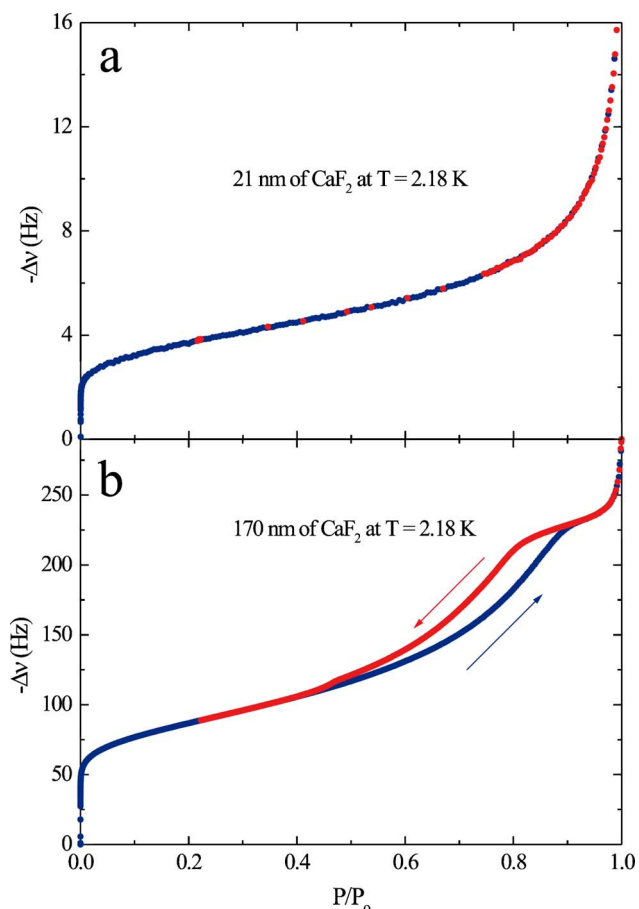


FIG. 10. (Color online) Forward (blue) and reverse (red) isotherms of normal helium ($T=2.18 \text{ K}$) on CaF₂ as a function of reduced pressure. (a) For thin CaF₂ substrates, forward and reverse isotherms are indistinguishable, even though the substrate area is several times that of a flat plate. (b) For CaF₂ substrates thicker than approximately 43 nm, there is a clearly visible broad hysteresis loop.

CaF₂ samples thicker than 43 nm yielded isotherms similar to that shown in Fig. 10(b). The hysteresis loops are considerably broader and the forward and reverse branches are less parallel than those observed for porous gold. The average pore diameters for these samples are estimated in the way as for the porous Au (see Table II).

3. Tortuosity and superfluid response

In geometries which deviate significantly from a flat plate, the interpretation of the frequency shift and dissipation signals which characterize superfluid onset is complicated by the effects of tortuosity. On a rough or porous surface, even an ideal zero viscosity fluid will contribute to the hydrodynamic mass because of inertia and the boundary condition requiring zero normal velocity. The tortuosity is a geometric property of the substrate which can be measured. To avoid possible complications due to phase boundary motion in the partially filled hysteretic regime, our determination of the tortuosity is based on an analysis of the regions of the isotherms outside the hysteresis loop corresponding either to filled pores or a thin film with empty pores.

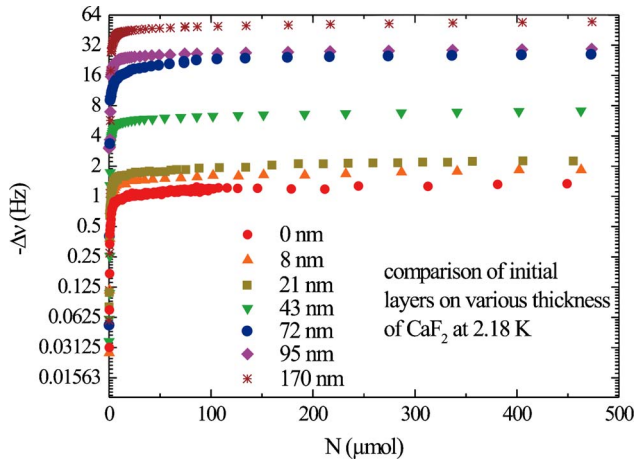


FIG. 11. (Color online) $\Delta\nu$ as a function of helium dosage N for CaF_2 substrates of various thicknesses at $T=2.18$ K. The rapid rise near $N=0$ is due to the formation of approximately two strongly bound layers of solidlike helium. The size of this rise is a measure of the area of the porous sample. Results for a nominally flat Au substrate are included for comparison.

The hydrodynamically coupled mass for a substrate with filled pores depends on temperature because the superfluid fraction of the bulk fluid depends on temperature. By comparing isotherms above the lambda point to isotherms at lower temperatures, the sensitivity of the oscillator response to superfluid can be determined. Comparison of isotherms on the same substrate at different temperatures is facilitated by plotting the frequency shift as a function of chemical potential offset from coexistence $\Delta\mu$ rather than pressure, as shown in Fig. 12, which shows data for a CaF_2 film of 170 nm nominal thickness. At low values of the chemical potential, the isotherms are essentially identical, since the coverage is a single valued function of the chemical potential and the adsorbed film is in the normal state and is viscously locked to the substrate. Once the liquid film becomes superfluid, the isotherms deviate from each other. The onset of superfluidity occurs at a value of the chemical potential offset $\Delta\mu_c$ that depends on temperature. There is, however, a threshold chemical potential below which the film remains normal even at $T=0$; this is the so-called dead layer. We have used low temperature isotherms to estimate the critical chemical potential for superfluid onset $\Delta\mu_{\text{solid}}$ to be approxi-

TABLE II. Average values for surface area, porosity, ε , average pore diameter, ζ , and superfluid drag coefficient, χ , of the six CaF_2 films and a flat Au surface.

Thickness (nm)	ε	Surface area (cm^2)	ζ (nm)	χ
0	Rough	0.74		0.04
8	Rough	1.03		0.24
21	Rough	1.33		0.55
43	0.32	4.27	13.4	0.52
72	0.38	14.47	7.54	0.60
95	0.40	17.87	7.48	0.66
170	0.43	33.17	8.78	0.7

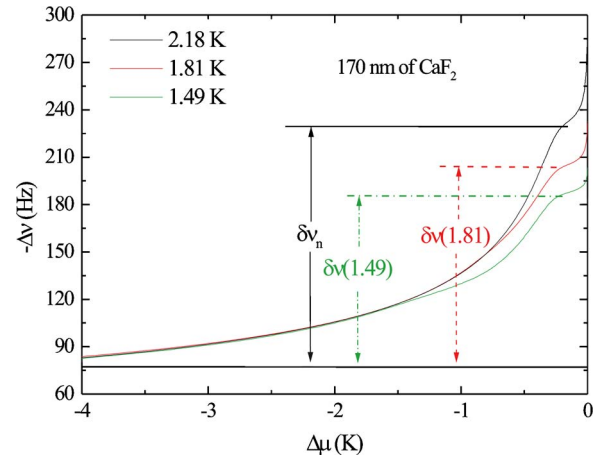


FIG. 12. (Color online) Frequency shift $\Delta\nu$ as a function of chemical potential offset $\Delta\mu$ for three forward isotherms on 170 nm of CaF_2 . The shoulder in each isotherm near $\Delta\mu=-0.5$ K represents the completion of pore filling. The horizontal line near $-\Delta\nu=75$ Hz is the completion of the solidlike layers. The frequency difference $\delta\nu$ between these two points is due to the hydrodynamically coupled fraction of the adsorbed liquid. At 2.18 K, the helium is normal, so all the adsorbed liquid contributes to the hydrodynamic mass. At lower temperatures, a fraction $(1-\chi)f_s(T)$ of the superfluid fraction, $f_s(T)$, decouples from the oscillator. The average χ measured in this way is 0.70.

mately -6.5 K. The frequency shift at this value of $\Delta\mu$ corresponds to adsorbed solid and must be subtracted from the total frequency shift to obtain the part due to adsorbed liquid. The frequency shift due to pores full of normal liquid helium at $T=2.18$ K is denoted as $\delta\nu_n$ in Fig. 12. At lower temperatures, for example, $T=1.81$ K, the frequency shift at pore filling is smaller, and is denoted by $\delta\nu(1.81)$. If the superfluid fraction completely decoupled from the oscillator, the ratio of $\delta\nu(1.81)/\delta\nu_n$ would simply be the normal fluid fraction at $T=1.81$ K which is approximately 0.32. In fact, the ratio is considerably higher, 0.83, which indicates that a fraction χ of the superfluid fraction also contributes to the inertia of the fluid. The fraction is computed from $0.83=0.32+\chi(1-0.32)$, so $\chi=0.75$. Figure 13 shows analogous data for a porous gold sample.

We have verified that the temperature dependence of the superfluid fraction with full pores corresponds to a conventional three-dimensional (3D) superfluid with a constant value of χ , as shown in Fig. 14.

A distinctly different method of measuring the superfluid drag coefficient for a porous substrate is to analyze the oscillator response in the vicinity of the superfluid transition at low temperatures and low helium coverages which are outside the hysteresis loop and where KT-type features are observed. The frequency shift due to superfluid onset is typically smaller on the porous or rough substrates than on a flat substrate of the same total area because some fraction of the superfluid is entrained and carried with the substrate. In this case, χ can be determined from a comparison of the observed frequency shift $\Delta\nu_{\text{porous}}$ in the porous substrate to the frequency shift $\Delta\nu_{\text{flat}}$ for a flat surface. χ is determined by minimizing the square of the quantity

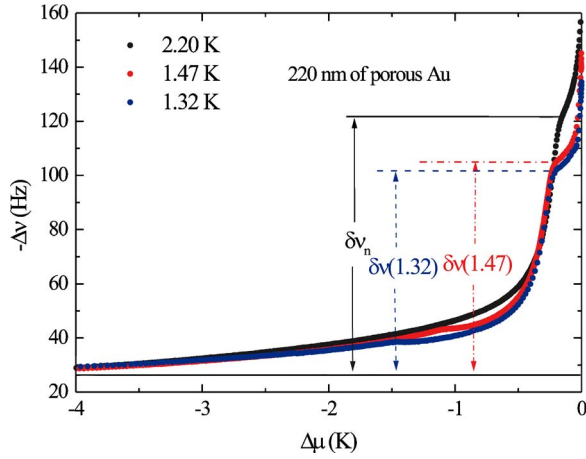


FIG. 13. (Color online) Frequency shift $\Delta\nu$ as a function of chemical potential offset $\Delta\mu$ for three forward isotherms on 220 nm of porous gold. The shoulder in each isotherm near $\Delta\mu = -0.5$ K represents the completion of pore filling. The horizontal line near $-\Delta\nu = 20$ Hz is the completion of the solidlike layers. The frequency difference $\delta\nu$ between these two points is due to the hydrodynamically coupled fraction of the adsorbed liquid. At 2.20 K, the helium is normal, so all the adsorbed liquid contributes to the hydrodynamic mass. At lower temperatures, a fraction $(1-\chi)f_s(T)$ of the superfluid fraction, $f_s(T)$, decouples from the oscillator. The average χ measured in this way is 0.71.

$$\Delta\nu_{\text{porous}} - \Delta\nu_{\text{flat}} A_r H(\Delta\mu - \Delta\mu_c)(1 - \chi), \quad (15)$$

where A_r is the ratio of the areas, H is the unit step function, and μ_c is the critical chemical potential. The porous surface areas are obtained from the data shown in Figs. 9 and 11. Figure 15 shows a typical example of this type of analysis for porous gold.

For thinner films of CaF_2 , there is no hysteresis and no feature in the isotherms associated with the full pore state, so

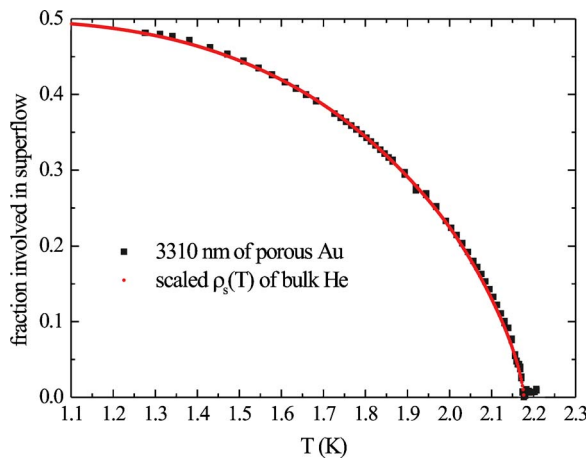


FIG. 14. (Color online) Black squares show the fraction of mass taking part in superflow with filled pores in 3310 nm of porous Au as a function of temperature. The red curve is the superfluid fraction of bulk helium, taken from Ref. 29, scaled by a factor of $(1-\chi)$, with $\chi=0.5$. The excellent agreement shows that helium in full pores behaves like a conventional 3D superfluid.

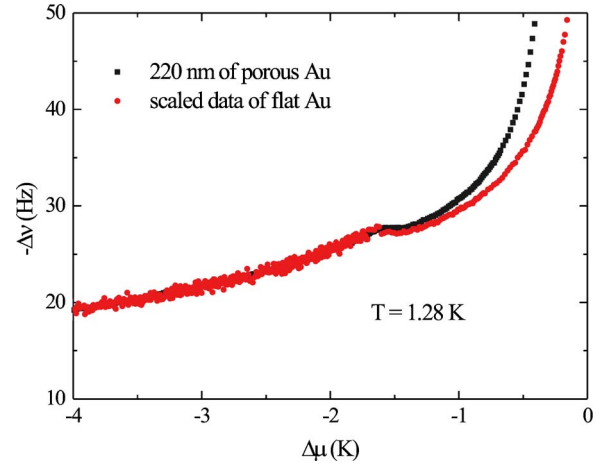


FIG. 15. (Color online) $\Delta\nu$ as a function of $\Delta\mu$ for 220 nm porous Au at $T=1.28$ K (black) compared to $\Delta\nu$ for a flat substrate scaled according to Eq. (15) (red). Setting $\chi=0.7$ gives a good fit in the vicinity of the transition; at higher values of $\Delta\mu$ the curves deviate because of the effects of capillary condensation.

the analysis of the KT-type features is the only available means of determining the superfluid drag coefficient. For the sample shown in Fig. 16, the drag coefficient is 0.24. A similar analysis for a number of CaF_2 samples shows that the superfluid drag increases with CaF_2 thickness until approximately 43 nm, and then becomes independent of thickness at a value of $\chi \sim 0.7$, as shown in Fig. 17.

These results can be summarized by stating that all of our porous gold samples, and all of the CaF_2 samples which are thick enough to exhibit hysteresis are characterized by a superfluid drag coefficient in the range of 0.5–0.7. The superflow through porous materials is often characterized by the tortuosity, τ , which can be related³⁰ to the drag coefficient by

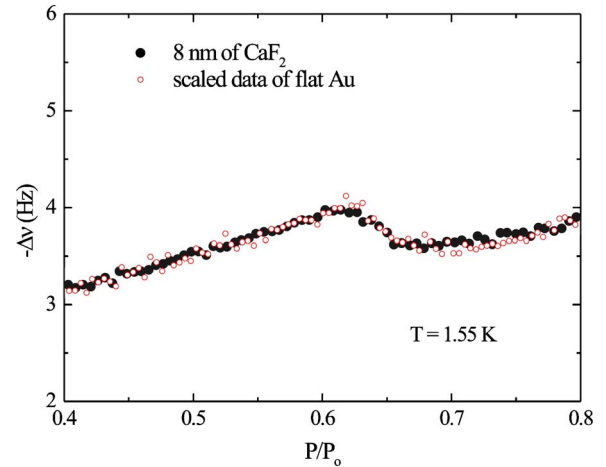


FIG. 16. (Color online) Frequency shift $\Delta\nu$ as a function of reduced pressure at $T=1.55$ K in the vicinity of the superfluid transition on thin (8 nm) CaF_2 (filled circles). The transition shows KT-type features. The open circles are data for a flat Au substrate scaled by an overall factor of 1.39 to account for the larger total area of the rough surface and by a factor of $(1-\chi)$ after the transition to account for the superfluid drag, as described by Eq. (15). A good fit is obtained with $\chi=0.24$.

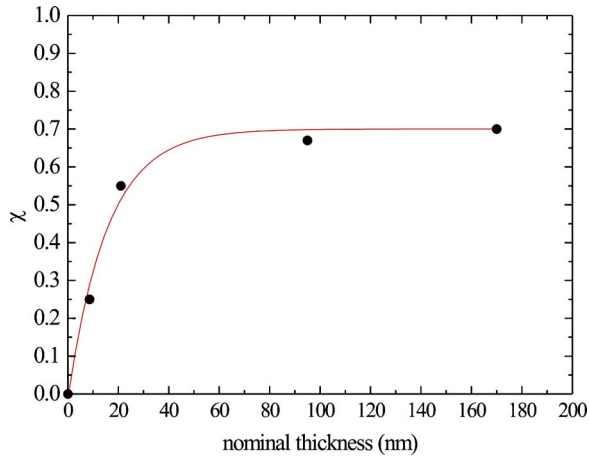


FIG. 17. (Color online) χ as a function of the nominal thickness of CaF_2 substrates. For thickness < 25 nm, χ is determined from KT features as shown in Fig. 16. For larger thicknesses, χ is determined by analyzing the behavior of full pores. The smooth curve is a guide to the eye.

$$\tau = \frac{1}{1 - \chi} \quad (16)$$

so our samples have a tortuosity in the range of 2–4. It is noteworthy that we obtain similar values of χ from an analysis of the superfluid transition at low helium coverage and low temperature with empty pores, and at high coverage and high temperature when the pores are full. This is in contrast to recent results in silica aerogel which show that χ is a strong function of the helium filling fraction, and ranges from almost 1 at low filling to approximately 0.2 with full pores.^{31,32}

III. SUPERFLUID AND CAPILLARY CONDENSATION TRANSITIONS

We have used the QCM to measure the conventional features of the KT transition, i.e., a frequency drop due to decoupling of the superfluid fraction, and a peak in the dissipation, for porous substrates. Figure 18 shows data at three different temperatures for the 95 nm thick CaF_2 sample, while Fig. 19 shows data for the 200 nm porous gold sample. The isotherms have been selected to illustrate the typical behavior of superfluid onset at low coverage, at high coverage when the pores are full, and at intermediate coverage where superfluid onset takes place within the hysteric region.

A noteworthy feature of Figs. 18 and 19 is that the dissipation peak which marks the onset of superfluidity is roughly the same size in all three regions, and in fact is very similar to the dissipation observed on a flat gold substrate as shown in Fig. 3. This is somewhat surprising because the total amount of helium in the porous samples is typically an order of magnitude larger than on the flat samples. In contrast, the frequency shift due to mass decoupling at the transition on porous materials, particularly inside the hysteric region, is much more subtle than on a flat surface. In some cases, it

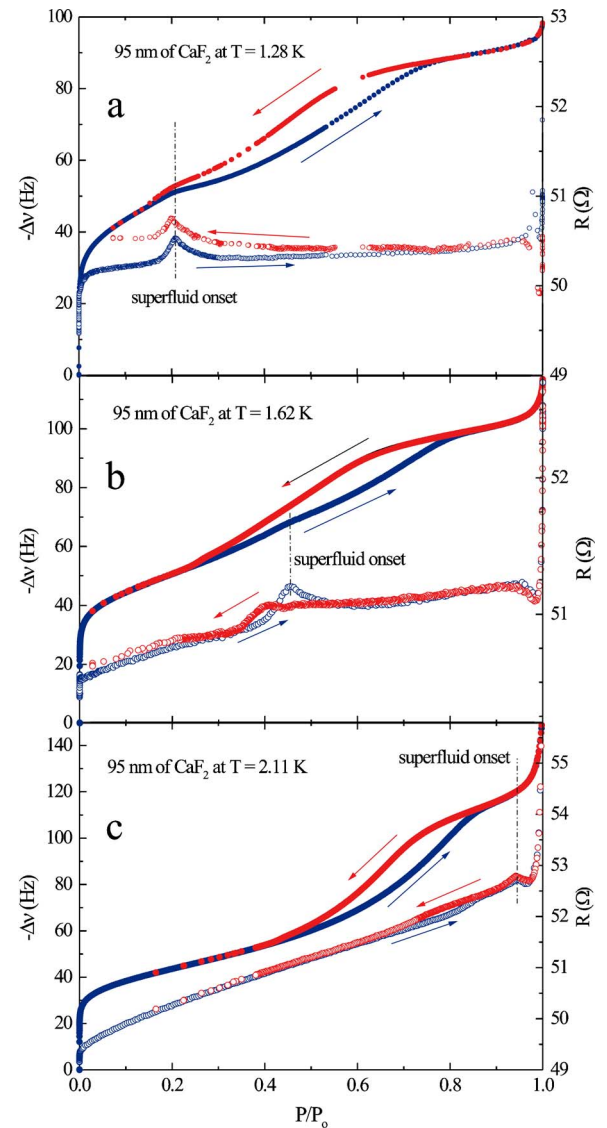


FIG. 18. (Color online) Forward and reverse isotherms of the frequency shift $\Delta\nu$ and the QCM resistance R on 95 nm of CaF_2 for three different temperatures: (a) $T=1.28$ K, (b) $T=1.62$ K, (c) $T=2.11$ K. The reduced pressure corresponding to superfluid onset is marked with a dashed line.

becomes difficult or impossible to locate the transition using only the $\Delta\nu$ signal. The fact that the $\Delta\nu$ signal of superfluid onset becomes difficult to locate experimentally has been noted previously.²⁸ We have used both the frequency shift and dissipation signatures of superfluid onset over a range of temperatures and chemical potentials to construct the phase diagrams shown in Figs. 20 and 29, which show the superfluid-normal boundary for porous gold and CaF_2 , respectively.

The main features of the porous gold phase diagram in Fig. 20 are the approximately horizontal triangular points which mark the endpoints of the hysteresis loops, and the circles and crosses which mark superfluid onset. The dotted curve shows the approximately quadratic relationship between $\Delta\mu$ and T expected for a flat gold substrate, as shown in Fig. 5. For a given temperature, superfluid onset occurs at

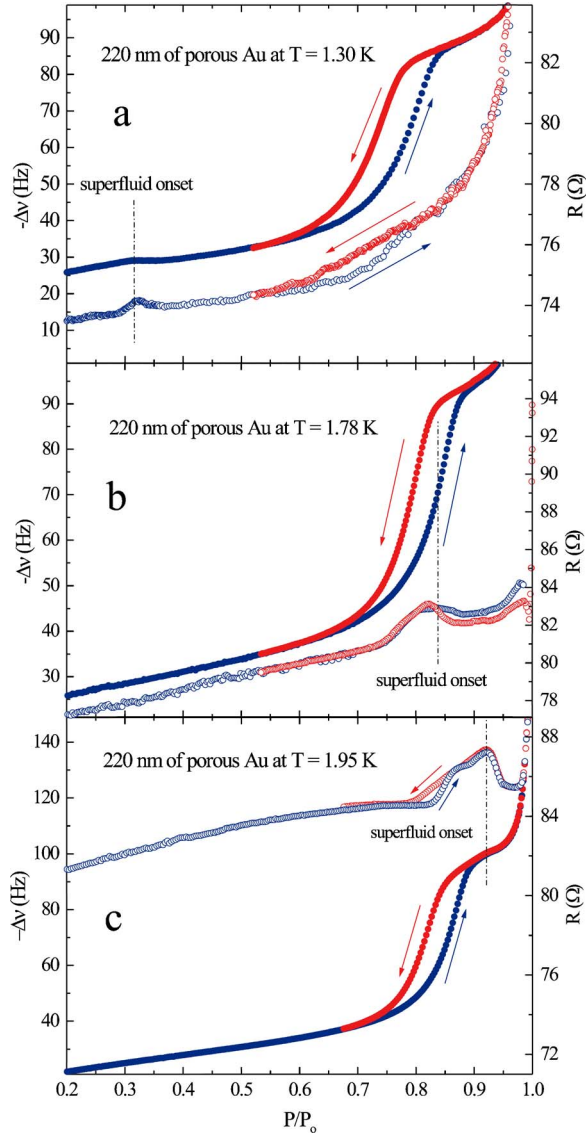


FIG. 19. (Color online) $\Delta\nu$ and dissipation R versus reduced pressure for helium adsorbed in 220 nm thick porous Au for (a) $T = 1.30$ K, (b) $T = 1.86$ K, (c) $T = 1.95$ K. A dashed vertical line marks the position of superfluid onset. In (a), superfluid onset occurs at a reduced pressure below the hysteresis loop and is marked by a peak in the dissipation and a slight change in slope of $\Delta\nu$; in (b) superfluid onset occurs in the middle of the hysteresis loop, and is marked by a broad peak in the dissipation, but no noticeable feature in $\Delta\nu$; in (c) superfluid onset occurs above the high pressure closing point of the hysteresis loop where the pores are full.

a slightly lower chemical potential in porous materials than on a flat substrate. Just as for flat substrates, superfluid onset occurs when the film thickness reaches the critical value given by Eq. (12). In a porous material, however, the relation between the adsorbed liquid film thickness and $\Delta\mu$ is more complicated because the effective potential is not simply proportional to d^{-3} , as in Eq. (10). Exact results for the chemical potential $\Delta\mu$ as a function of film thickness d have been worked out for a cylindrical pore of diameter ζ by Saam and Cole,³³

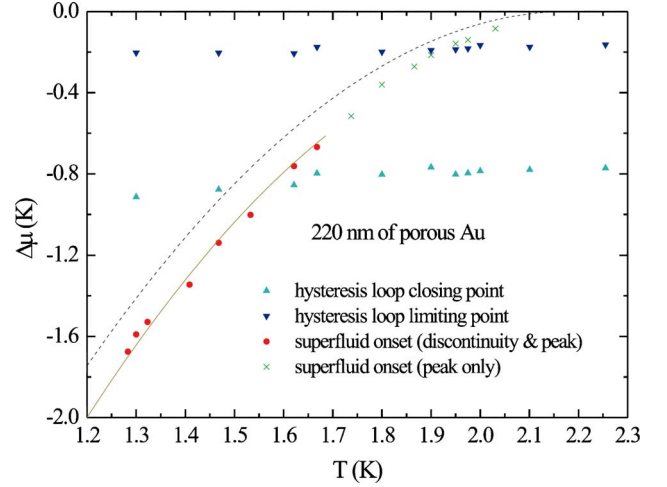


FIG. 20. (Color online) $\Delta\mu$ versus T phase diagram for helium in a 220 nm porous Au substrate, showing the limits of the hysteresis region (upward and downward pointing triangles) and the superfluid or normal boundary (circles and crosses). The dashed line represents the normal-superfluid boundary on flat Au as appears in Fig. 5. The superfluid onset in porous Au below capillary condensation has both KT features at the transition point. The curve passing through these points is the prediction for the location of the superfluid transition based on Eq. (16) as described in the text. The curve ends at the capillary instability. For chemical potentials and temperatures higher than the endpoint, only dissipation peaks mark the superfluid transition (crosses).

$$\Delta\mu = -\frac{12\pi\alpha}{\zeta^3} F_{2,1}\left(\frac{3}{2}, \frac{5}{2}; 1; y^2\right) - \frac{2\sigma_{lg}v_l}{k_B(\zeta - 2d)}, \quad (17)$$

where y is $1 - 2d/\zeta$, d represents the film thickness along the pore wall, $F_{2,1}$ is a hypergeometric function, σ_{lg} is the surface tension, v_l is the volume per atom in the liquid, k_B is Boltzmann's constant, and α is the van der Waals constant, equal to $3100 \text{ K } \text{\AA}^3$.²² Using the previously determined pore diameter ζ (see Table I), Eq. (17) provides a relation between $\Delta\mu$ and d with no free parameters. Simultaneous solution of Eqs. (10), (12), and (17) with $\zeta = 22 \text{ nm}$ yields a relation between the onset chemical potential $\Delta\mu_c$ and the temperature T which is shown as the dashed curve in Fig. 20. It provides a very accurate description of the location of the superfluid transition in the porous gold samples.

For a given pore diameter ζ , the relationship between $\Delta\mu$ and d described by Eq. (17) will become multivalued for sufficiently small $\Delta\mu$; this is a manifestation of the capillary instability of films in a pore. Using Eq. (17) to model hysteresis loops in real materials with a distribution of pore sizes requires some kind of averaging procedure. We have computed the instability limit for a range of pore sizes and then averaged over a Gaussian distribution characterized by a mean pore diameter ζ_A and a standard deviation 2Δ using Eqs. (3.66) and (3.67) of Ref. 33. The model assumes that the pores are independent, and that the adsorption section of the isotherm follows the metastable thin film branch of solutions until the spinodal instability is reached. The results of this analysis for a typical porous gold sample is shown in Fig. 21.

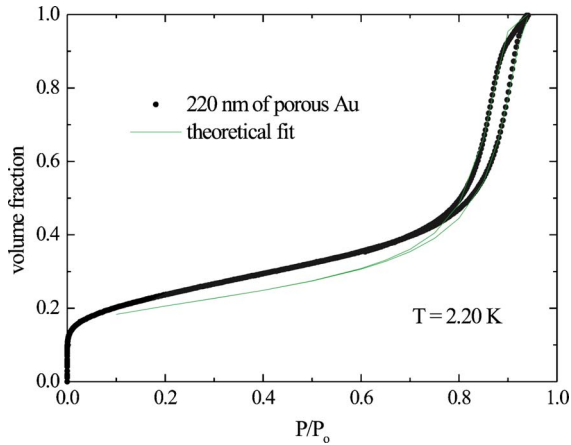


FIG. 21. (Color online) Comparison of measured isotherm in 220 nm of porous Au at $T=2.20$ K (black circles) and a theoretical sorption isotherm calculated using the model described in Ref. 33 (green line). The isotherms are normalized to unity at the pore filling limit of the hysteresis loop. The fitting parameters used in the Gaussian distribution function are $\zeta_A=18.2$ nm and $2\Delta=2.2$ nm giving pore diameters around 20 nm, relatively close to the measurements made using the response of the QCM.

Figure 21 shows the total amount of fluid in the porous medium. Some of this fluid is in the form of a thin film on the walls of the larger pores, while some of the smaller pores are beyond the stability limit and are filled with fluid. The model allows us to estimate the contribution from each source separately. Figure 22 shows the fraction of filled pores as a function of P/P_0 . It is interesting to note that even in the range of P/P_0 near the lower closing point of the hysteresis loop, there are already a substantial number of filled pores.

Next we will discuss the superfluid transitions in CaF_2 . The phase diagram on CaF_2 depends sensitively on the thickness of the porous substrate because of the previously mentioned transition from a rough to porous structure. This is in contrast to the phase diagram of porous Au as shown in Fig. 20, which is qualitatively the same for all the porous Au samples that we studied. On thin substrates of CaF_2 , which do not have hysteresis, isotherms have both the frequency

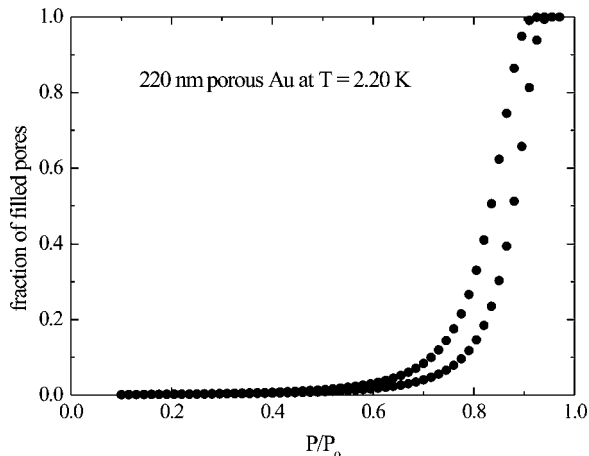


FIG. 22. Percentage of pores filled in 220 nm of porous Au at $T=2.20$ K computed from the model of Ref. 33.

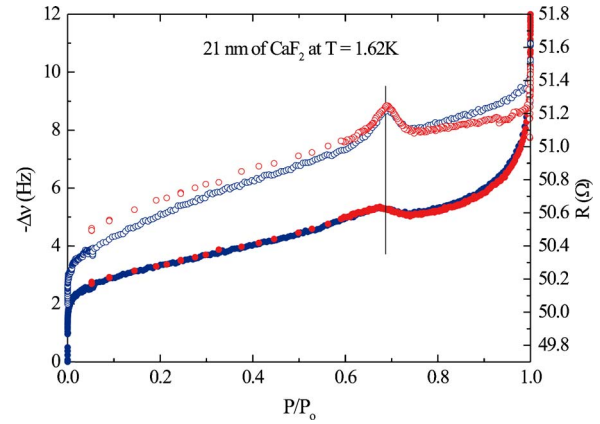


FIG. 23. (Color online) Forward and reverse $\Delta\nu$ and R isotherms on 21 nm of CaF_2 at $T=1.62$ K showing no hysteresis, with broadened KT-type features at the superfluid transition.

discontinuity and dissipation peak characteristic of a KT transition, as shown in Fig. 23. The superfluid transition can be quantitatively explained by taking into account the increase in surface area of the substrate and the value of the superfluid drag coefficient as seen in Fig. 16.

Isotherms on CaF_2 substrates greater than 43 nm in thickness display hysteresis, and the superfluid transitions no longer have conventional KT features. Figure 24 compares the frequency shift near the superfluid transition on the 95 nm CaF_2 substrate to a flat Au surface scaled using Eq. (15), which accounts for the increased area and the tortuosity. It is clear from the comparison that the frequency shift associated with the superfluid onset cannot be quantitatively explained using KT analysis. The frequency shift has no hint of a discontinuity at the transition, but rather has a barely discernible and gradual change in slope. Figure 25 presents another view of the transition region on the same CaF_2 substrate, and shows the forward and reverse branches of the

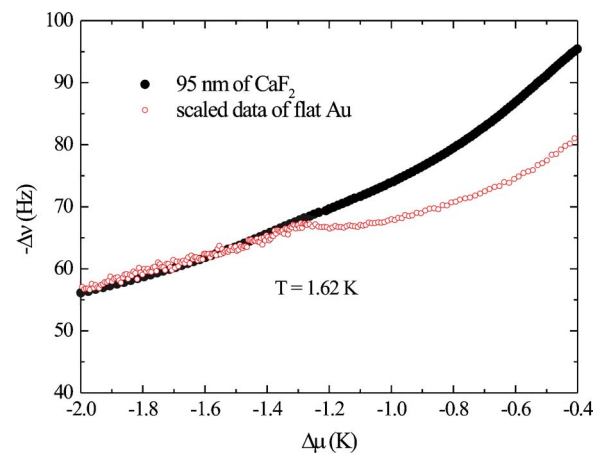


FIG. 24. (Color online) Comparison of the frequency shift isotherm for $T=1.62$ K on 95 nm CaF_2 [solid (black) circles] and the expected KT frequency shift based on scaling the flat substrate data using Eq. (15) to account for the 22-fold increase in area and the measured drag coefficient $\chi=0.7$ [open (red) circles]. Note that the scaled KT transition is qualitatively different from the transition in CaF_2 .

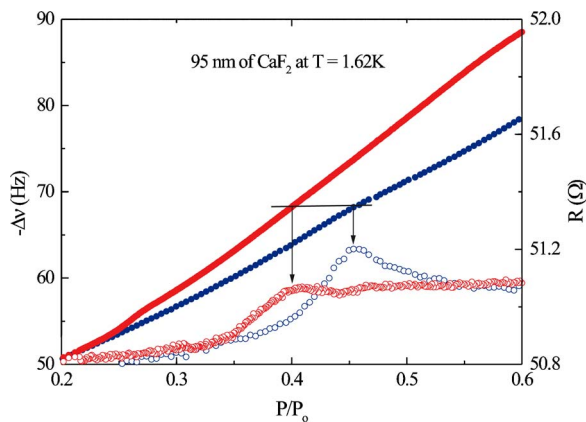


FIG. 25. (Color online) Forward (blue) and reverse isotherms (red) of frequency shift $-\Delta\nu$ (upper curves, left-hand scale) and dissipation R (lower curves, right-hand scale) on 95 nm of CaF_2 at 1.62 K. The frequency shift is very smooth through the transition, but the dissipation shows clear peaks. The dissipation is hysteretic in pressure, but the peaks which mark the transition correspond to the same frequency shift, indicating that the transition is determined by the coverage and not the pressure.

isotherm for both the frequency shift and the dissipation. Both branches of the frequency shift are smooth and have only very subtle features at the transition. In contrast, the dissipation has clearly identifiable peaks at the transition. The separation of the peaks shows that the transition is hysteretic, but the transition occurs on both the adsorption and desorption branches at the same value of the frequency shift, i.e., the same total helium coverage. Figure 26 shows that the superfluid transition in porous Au within the hysteresis loops is also smooth and contains no features or discontinuities on the scale predicted by the KT theory.

Figures 24 and 25 show that in the hysteretic regime on porous CaF_2 , the amount of fluid which decouples from the QCM does not change abruptly at the transition and does not

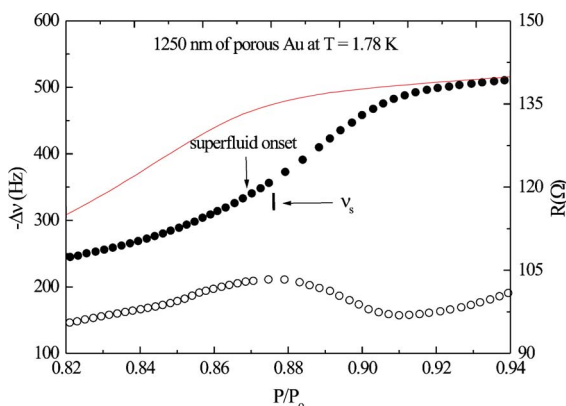


FIG. 26. (Color online) $\Delta\nu$ (filled circles) and R (open circles) adsorption isotherms at $T=1.78$ K in 1250 nm of porous Au. Red curve shows the desorption branch of $\Delta\nu$. Although there is a peak in the dissipation, there is no corresponding feature in $\Delta\nu$. The expected size of the feature is indicated by the length of the ν_s line, 15 Hz, which is estimated by using the KT value for a flat Au substrate scaled by a factor of 45, to take into account the increase in area, and reduced by $(1-\chi)$, where χ is 0.68.

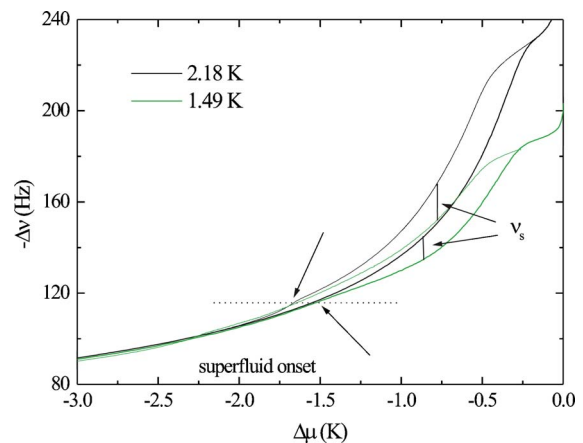


FIG. 27. (Color online) Forward and reverse isotherm on 170 nm of CaF_2 at 2.18 K (black) and 1.49 K (green). In the chemical potential range where the helium is normal, the isotherms coincide, but they separate at superfluid onset of the 1.49 K isotherm. Superfluid onset takes place for different values of $\Delta\mu$ but the same coverage on the forward and reverse branches. In both cases, the onset of superflow is characterized by a smooth, continuous separation from the normal isotherm.

grow with coverage or chemical potential as it does on a flat substrate. Since the frequency shift at the transition is smooth and gradual, the extrapolation procedure used to determine the superfluid density on a flat substrate, shown in Fig. 3, does not yield meaningful results. One method of highlighting the effects of superfluidity is to carefully measure the difference between the frequency shifts observed in the normal state with $T > T_\lambda$ to the frequency shifts observed with $T < T_\lambda$, using data like those shown in Fig. 12 and Fig. 27 plotted as a function of $\Delta\mu$.

The adsorbed film thickness of a wetting fluid on a flat substrate is a single valued function of the chemical potential offset $\Delta\mu$, and does not depend on the pressure or temperature separately, so the frequency shift at different temperatures but identical values of $\Delta\mu$ should coincide. As shown in the figures, this is also the case for CaF_2 substrates at low coverage, but above the critical coverage, the curves deviate from each other. The difference between the frequency shift in the normal state $-\Delta\nu_{2.18}(\Delta\mu)$ and the superfluid state at temperature T , $-\Delta\nu_T(\Delta\mu)$, is due to the decoupled superfluid mass, and the fractional difference n_s ,

$$n_s = \frac{\Delta\nu_T(\Delta\mu_c) - \Delta\nu_T(\Delta\mu)}{\Delta\nu_{2.18}(\Delta\mu) - \Delta\nu_{2.18}(\Delta\mu_{\text{solid}})} \quad (18)$$

is a measure of the fraction of the pore fluid which participates in superflow. Plots of n_s as a function of $\Delta\nu_T(\Delta\mu_c) - \Delta\nu_T(\Delta\mu)$, where $\Delta\nu_T(\Delta\mu_c)$ is the critical frequency shift corresponding to onset of superflow, are shown for both the forward and reverse branches for two different temperatures in Fig. 28. The plot shows that the superflow fraction n_s increases from zero in a smooth way which can be approximately described by a power law. The exponent of $\Delta\nu_T(\Delta\mu_c) - \Delta\nu_T(\Delta\mu)$ is slightly greater in the forward direc-

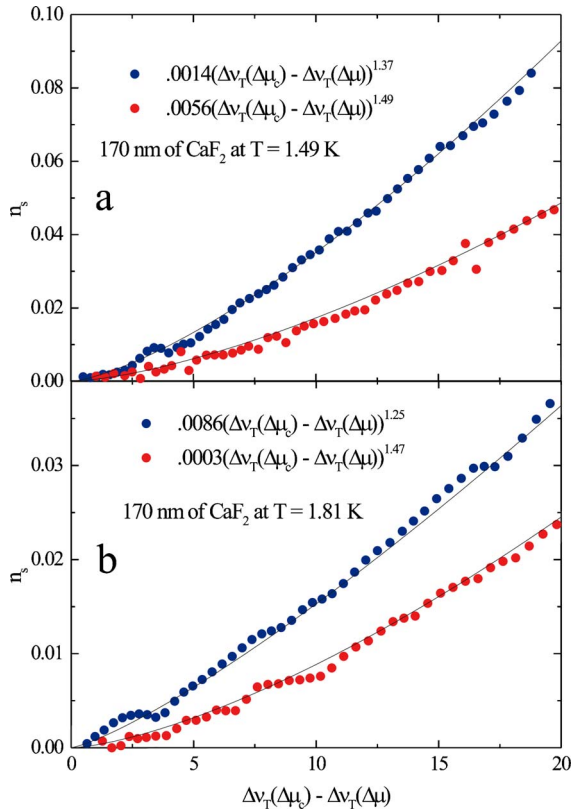


FIG. 28. (Color online) Superflow fraction as a function of $\Delta\nu_c - \Delta\nu$, where $\Delta\nu_c$ is the frequency shift at onset in 170 nm CaF_2 substrate for (a) $T = 1.49$ K and (b) $T = 1.81$ K. For each temperature, n_s is calculated by subtracting the frequency shift at that temperature from the isotherm at 2.18 K, as shown in Fig. 27. The exponents of best power law fits are shown in the insets, where the forward is in blue, and the reverse in red.

tion than in the reverse direction, and ranges from approximately 1.3 to 1.8.

The peak in the dissipation and the gradual deviation of the superfluid and normal frequency shift which occurs at $\Delta\mu_c$ does not have the conventional characteristics of either a 3D or 2D superfluid transition of a homogeneous phase. The position of this feature is shown in a $\Delta\mu$ - T phase diagram in Fig. 29. Note that for the temperature range accessible in our apparatus, the superfluid transition in CaF_2 always takes place inside the hysteresis loop.

Just as for porous gold, the Saam and Cole³³ model can be used to calculate the shape of both the adsorption and desorption branches of the isotherm. A typical example of the comparison of the model to the data is shown in Fig. 30. In order to describe the broad hysteresis loops in CaF_2 , the width of the pore distribution $2\Delta = 6.2$ nm must be chosen larger than the mean pore diameter $\zeta_A = 4.2$ nm.

IV. DISCUSSION AND CONCLUSION

The phase diagrams shown in Figs. 20 and 29 can be used to formulate a general picture of superfluid onset in porous media. If superfluid onset occurs on the low coverage portion of the isotherm where the coverage is a unique single valued

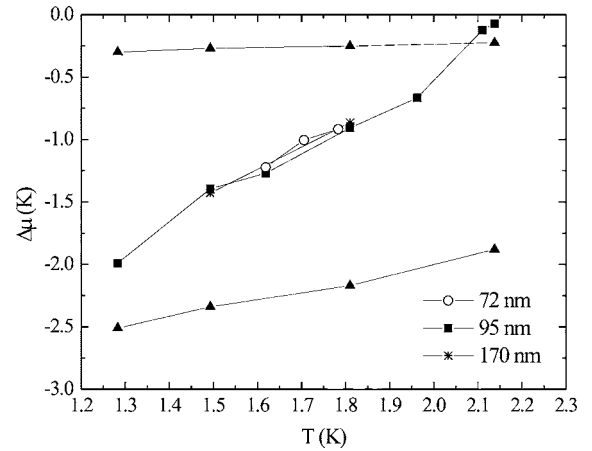


FIG. 29. Phase diagram of helium in CaF_2 for samples thick enough to show hysteresis. The endpoints of the hysteresis loops are denoted by triangles. The position of the dissipation peak is marked by circles, squares and crosses.

nonhysteretic function of the chemical potential, the superfluid transition is a conventional 2D KT transition characterized by a peak in the dissipation and an abrupt drop in the hydrodynamic mass coupled to the oscillator. The size and shape of the frequency shifts can be described using KT theory corrected for the increased area and the tortuosity of the substrate. The critical thickness, or the equivalent critical chemical potential, at which superfluid onset occurs can be described by the simple linear relation between thickness and the correlation length shown in Fig. 6 which expresses the fact that the film becomes superfluid once its total thickness exceeds the correlation length plus an inert layer thickness of approximately 0.7 nm. The locus of transition points on a nominally flat surface form an approximately quadratic curve in the $\Delta\mu$ - T plane. In a porous medium in the low coverage regime, the transition points fall on a similar curve which is slightly displaced to lower chemical potentials. The shift in

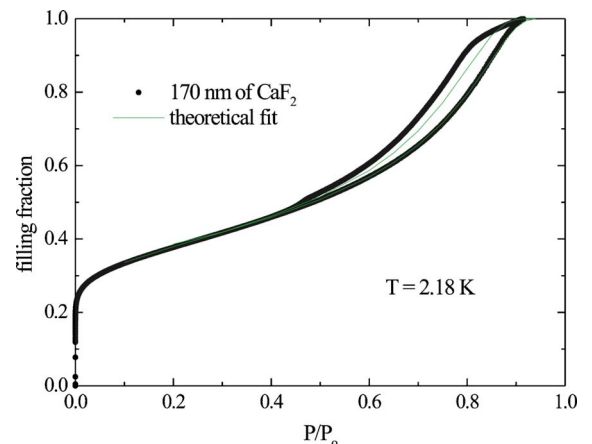


FIG. 30. (Color online) Comparison of measured isotherm on 170 nm of CaF_2 at 2.18 K (black circles) and a theoretical sorption isotherm using the model described in Ref. 33 (green line). The isotherms are normalized to unity at the pore filling limit of the hysteresis loop. The fitting parameters are $\zeta_A = 4.2$ nm and $2\Delta = 6.2$ nm.

onset chemical potential can be quantitatively predicted using the theory of Saam and Cole.³³

As the temperature is raised, the coverage required for superfluid onset also rises and eventually enters the regime where the coverage is a hysteretic function of the pressure and the chemical potential. It is important to note that the hysteretic regime is not announced by any obvious experimental marker on the adsorption isotherm, and the only practical way to determine the threshold coverage is to explicitly construct the hysteresis loop using a desorption isotherm. If superfluid onset occurs in this regime, the dissipation signature is unchanged from the low coverage behavior; it is approximately the same size and follows the same trajectory through the $\Delta\mu$ - T plane. This suggests that some aspect of the transition even in the hysteretic regime is still determined by the 2D criterion $d_c \sim d_0 + \xi(T)$. In contrast, the frequency shift due to hydrodynamic mass decoupling is drastically different in the hysteretic regime. In place of the nearly discontinuous step characteristic of the KT transition, the frequency shift isotherms of a porous medium in the hysteretic regime are smooth with a gradual and sometimes imperceptible change in slope. Once the pores are full, however, the temperature dependence of the frequency shift of the saturated medium behaves like a bulk 3D superfluid. This seems to suggest that the helium makes a transition from a normal state at low coverage to a conventional bulk superfluid at pore filling in a smooth and continuous way, which is quite unusual. In the case of CaF_2 , the hysteresis loops are broad enough that we can directly determine the amount of hydrodynamically decoupled mass by comparison with isotherms above T_λ . The decoupled mass scales as $[\Delta\nu_T(\Delta\mu_c) - \Delta\nu_T(\Delta\mu)]^k$, where $[\Delta\mu_c, \Delta\nu_T(\Delta\mu_c)]$ defines the position of the dissipation peak, and k is in the range 1.3–1.8. The exponents are slightly higher on the forward branch when the transition is from normal to super, and slightly lower on the reverse branch when the transition is from super to normal. We believe that superfluid onset in porous Au obeys a similar scaling, but it is considerably more difficult to perform an accurate subtraction because the isotherms are much steeper and the closing points of the hysteresis loop depend more strongly on temperature.

The superfluid onset phenomena we observe in the hysteretic two phase region may be related to recent observations of filling of aerogel^{34,35} which show that the distribution of fluid is highly inhomogeneous and consists of isolated nanometer scale droplets which grow and eventually merge. This picture is also supported by the results shown in Fig. 22, which shows that a considerable fraction of the pores are full even at the lower end of the hysteresis loop. If the droplets are larger than the bulk correlation length, they are presumably superfluid, but our measurements suggest that they are pinned and move with the porous substrate, as shown in the schematic of Fig. 31. The superfluid transitions of these droplets would not be expected to be accompanied by a dissipation peak because the film in these pores never has the critical thickness, but rather makes a discontinuous jump from the normal state below d_c to a superfluid filled pore;



FIG. 31. (Color online) Cartoon of a porous structure (yellow) with regions covered by thin helium films (light blue), regions covered by bulk liquid droplets (blue), and helium vapor (white). The figure represents a state within a hysteresis loop where bulklike liquid forms in narrower regions due to capillary condensation. The liquid coexists with a thin film which covers the surface of the wider regions. The bulklike liquid regions have a characteristic scale larger than the correlation length and will be superfluid, while the thin films will remain normal. This model implies the existence of a complicated network of superfluid-normal boundaries inside the porous structure. In this picture, the superfluid-normal boundaries are pinned and, therefore, do not contribute to the standard superfluid signatures. A dissipation peak and the start of gradual unloading of mass are seen only when superfluidity percolates via the thin films within the structure, allowing for superflow.

this is similar to the situation which occurs when the KT transition collides with the prewetting transition.³⁶

Outside the filled pores, the walls of the porous medium are covered with a film whose thickness depends on the chemical potential. At low values of the chemical potential, the film will be thinner than a correlation length and will be normal. At a critical value of the chemical potential which can be computed using the theory of Ref. 33, the film will become superfluid and superflow between droplets becomes possible. This essentially 2D transition in the film is a candidate mechanism for the dissipation features we observe which closely track the transitions on a flat substrate in the $\Delta\mu$ - T plane. The effective hydrodynamic mass of this network of droplets and films is presumably determined by its connectivity properties which may undergo a percolation-like transition at a critical coverage.^{37–39} It is interesting to note that the range of exponents we observe is similar to those expected for the hydraulic conductivity of conventional viscous flow in porous media, although the fundamental dynamics of superflow through the medium is presumably quite different.

ACKNOWLEDGMENTS

The authors thank J. E. Rutledge and J. C. Burton for useful discussions. This work was supported by NASA Contract No. NAG8-1437 and NSF Grant No. DMR 0509685.

- ¹N. Mulders and J. R. Beamish, Phys. Rev. Lett. **62**, 438 (1989).
- ²J. C. Herrmann and R. B. Hallock, Phys. Rev. B **68**, 224510 (2003).
- ³C. W. Kiewiet, H. E. Hall, and J. D. Reppy, Phys. Rev. Lett. **35**, 1286 (1975).
- ⁴M. Revzen, B. Shapiro, C. G. Kuper, and J. Rudnick, Phys. Rev. Lett. **33**, 143 (1974).
- ⁵G. A. Williams, R. Rosenbaum, and I. Rudnick, Phys. Rev. Lett. **42**, 1282 (1979).
- ⁶M. P. Lilly, A. H. Wootters, and R. B. Hallock, Phys. Rev. B **65**, 104503 (2002).
- ⁷A. H. Wootters and R. B. Hallock, J. Low Temp. Phys. **121**, 549 (2000).
- ⁸M. H. W. Chan, K. I. Blum, S. Q. Murphy, G. K. S. Wong, and J. D. Reppy, Phys. Rev. Lett. **61**, 1950 (1988).
- ⁹C. Ashton, S. Babuin, and A. I. Golov, J. Low Temp. Phys. **138**, 183 (2005).
- ¹⁰G. M. Zassenhaus, A. D. Corwin, and J. D. Reppy, Physica B **284**, 111 (2000).
- ¹¹J. R. Beamish and T. Herman, J. Low Temp. Phys. **134**, 339 (2004).
- ¹²M. Hieda, A. C. Clark, and M. H. W. Chan, J. Low Temp. Phys. **134**, 91 (2004).
- ¹³G. Sauerby, Z. Phys. **155**, 206 (1959).
- ¹⁴L. Bruschi, G. Delfitto, and G. Mistura, Rev. Sci. Instrum. **70**, 153 (1999).
- ¹⁵*Vacuum Microbalances Techniques*, 5th ed., edited by C. D. Stockbridge (Plenum, New York, 1966).
- ¹⁶J. M. Kosterlitz and D. J. Thouless, J. Phys. C **6**, 1181 (1973).
- ¹⁷M. Chester, J. B. Stevens, and L. C. Yang, Phys. Rev. Lett. **29**, 211 (1972).
- ¹⁸M. Chester and L. C. Yang, Phys. Rev. Lett. **31**, 1377 (1973).
- ¹⁹V. Ambegaokar, B. I. Halperin, D. R. Nelson, and E. D. Siggia, Phys. Rev. B **21**, 1806 (1980).
- ²⁰R. Brada, H. Chayet, and W. I. Glaberson, Phys. Rev. B **48**, 12874 (1993).
- ²¹B. D. Josephson, Phys. Lett. **21**, 608 (1966).
- ²²E. Cheng and M. W. Cole, Phys. Rev. B **38**, 987 (1988).
- ²³E. S. Sabisky and C. H. Anderson, Phys. Rev. Lett. **30**, 1122 (1973).
- ²⁴J. Maps and R. B. Hallock, Phys. Rev. B **27**, 5491 (1983).
- ²⁵R. W. A. van de Laar, A. van der Hoek, and H. van Beelen, Physica B **216**, 24 (1995).
- ²⁶V. E. Syvokon, Low Temp. Phys. **32**, 48 (2006).
- ²⁷K. S. W. Sing, D. H. Everett, R. A. W. Haul, L. Moscou, R. A. Pierotti, J. Rouquerol, and T. Siemieniewska, Pure Appl. Chem. **57**, 603 (1985).
- ²⁸D. R. Luhman and R. B. Hallock, Phys. Rev. Lett. **93**, 086106 (2004).
- ²⁹R. J. Donnelly and C. F. Barenghi, J. Phys. Chem. Ref. Data **27**, 1217 (1998).
- ³⁰D. L. Johnson and P. N. Sen, Phys. Rev. B **24**, 2486 (1981).
- ³¹R. Dolesi, M. Bonaldi, and S. Vitale, J. Low Temp. Phys. **118**, 219 (2000).
- ³²A. I. Golov, I. B. Berkutov, S. Babuin, and D. J. Cousins, Physica B **328**, 258 (2003).
- ³³W. F. Saam and M. W. Cole, Phys. Rev. B **11**, 1086 (1975).
- ³⁴T. Lambert, C. Gabay, L. Puech, and P. E. Wolf, J. Low Temp. Phys. **134**, 293 (2004).
- ³⁵W. Miyashita, K. Yoneyama, R. Nomura, and Y. Okuda, J. Phys. Chem. Solids **66**, 1509 (2005).
- ³⁶P. Taborek and J. E. Rutledge, Phys. Rev. Lett. **71**, 263 (1993).
- ³⁷B. Berkowitz and D. P. Hansen, Transp. Porous Media **45**, 303 (2001).
- ³⁸B. Berkowitz and I. Balberg, Transp. Porous Media **9**, 275 (1992).
- ³⁹A. G. Hunt, Philos. Mag. **85**, 3409 (2005).